

Mountain waves over the Hohe Tauern: Influence of upstream diabatic effects

By JAMES D. DOYLE^{1*} and RONALD B. SMITH²

¹*Naval Research Laboratory, Monterey, USA*

²*Yale University, New Haven, USA*

(Received 13 December 2001; revised 10 June 2002)

SUMMARY

The structure and intensity of large-amplitude trapped lee waves over the Hohe Tauern range of the Alps on 20 September 1999 are investigated through the analysis of *in situ* aircraft observations, airborne lidar, Global Positioning System dropsondes, rapid-scan satellite imagery, and a suite of linear and nonlinear model simulations. Observations indicate that the lee waves attained a maximum vertical velocity of more than 9 m s^{-1} , potential-temperature perturbations greater than 10 K, and a horizontal wavelength of approximately 12–15 km. High-resolution nonlinear simulations accurately capture the trapped-wave evolution and characteristics. Blocking of the southerly flow upstream of the Hohe Tauern decreases the depth of the layer that ascends the mountain crest, and modulates the wave response. Vertically propagating waves are partially ducted into a train of lee waves as a result of weak stability aloft, which forms due to diabatic processes associated with precipitation upstream of the Hohe Tauern crest. Linear analytic solutions confirm the importance of the weak-stability layer in the upper-troposphere for the development of the non-hydrostatic evanescent waves. Results from idealized two-dimensional nonlinear simulations suggest that the vertical depth of diabatic heating associated with the upstream precipitation is important. In this case, latent heating over a relatively shallow depth tunes the atmosphere for a nonlinear resonance that leads to strong descent in the lee and reinforcement of the lee waves.

KEYWORDS: Gravity waves Mesoscale Alpine Programme Numerical modelling

1. INTRODUCTION

When stably stratified air flows over a topographic obstacle, energy is radiated away from the barrier by internal gravity waves, more commonly referred to as mountain waves. One of the fundamental questions concerning the influence of mountain waves on the atmosphere relates to whether the energy propagates vertically or is dispersed horizontally beneath a wave duct. Hydrostatic mountain waves propagate vertically directly above a topographic barrier and exhibit an upstream phase tilt (Smith 1979). Vertically propagating waves can be trapped by a wave-guide that forms when the wind speed and/or static stability of the incident airstream varies rapidly with height (e.g. Scorer 1949). Trapped lee waves are composed of a superposition of two non-hydrostatic gravity waves, one of which propagates upwards and a second that is downward propagating yielding vertically oriented phase lines (Durrán 1990). Trapped lee waves typically have horizontal wavelengths shorter than those of hydrostatic mountain waves. In the complex flows that occur in nature, wave ducts are typically imperfect and permit longer wavelengths to propagate vertically through the wave guides (e.g. Bretherton 1969; Shutts 1992; Shutts and Broad 1993). The momentum transport associated with vertically propagating waves is large enough to modulate the atmospheric general circulation (e.g. Bretherton 1969).

Numerical models have often been an integral part of the study of mountain-wave dynamics. A number of recent studies have used high-resolution models with realistic topography to accurately simulate the basic characteristics of trapped mountain waves, such as the wavelength, amplitude and position, for many diverse locations including

* Corresponding author: Naval Research Laboratory, Marine Meteorology Division, 7 Grace Hopper Avenue, Monterey, CA 93943-5502 USA. e-mail: doyle@nrlmry.navy.mil

Report Documentation Page			Form Approved OMB No. 0704-0188		
Public reporting burden for the collection of information is estimated to average 1 hour per response, including the time for reviewing instructions, searching existing data sources, gathering and maintaining the data needed, and completing and reviewing the collection of information. Send comments regarding this burden estimate or any other aspect of this collection of information, including suggestions for reducing this burden, to Washington Headquarters Services, Directorate for Information Operations and Reports, 1215 Jefferson Davis Highway, Suite 1204, Arlington VA 22202-4302. Respondents should be aware that notwithstanding any other provision of law, no person shall be subject to a penalty for failing to comply with a collection of information if it does not display a currently valid OMB control number.					
1. REPORT DATE 10 JUN 2002		2. REPORT TYPE		3. DATES COVERED 00-00-2002 to 00-00-2002	
4. TITLE AND SUBTITLE Mountain waves over the Hohe Tauern: Influence of upstream diabatic effects			5a. CONTRACT NUMBER		
			5b. GRANT NUMBER		
			5c. PROGRAM ELEMENT NUMBER		
6. AUTHOR(S)			5d. PROJECT NUMBER		
			5e. TASK NUMBER		
			5f. WORK UNIT NUMBER		
7. PERFORMING ORGANIZATION NAME(S) AND ADDRESS(ES) Naval Research Laboratory, 7 Grace Hopper Ave., Stop 2, Monterey, CA, 93943-5502			8. PERFORMING ORGANIZATION REPORT NUMBER		
9. SPONSORING/MONITORING AGENCY NAME(S) AND ADDRESS(ES)			10. SPONSOR/MONITOR'S ACRONYM(S)		
			11. SPONSOR/MONITOR'S REPORT NUMBER(S)		
12. DISTRIBUTION/AVAILABILITY STATEMENT Approved for public release; distribution unlimited					
13. SUPPLEMENTARY NOTES					
14. ABSTRACT					
15. SUBJECT TERMS					
16. SECURITY CLASSIFICATION OF:			17. LIMITATION OF ABSTRACT Same as Report (SAR)	18. NUMBER OF PAGES 25	19a. NAME OF RESPONSIBLE PERSON
a. REPORT unclassified	b. ABSTRACT unclassified	c. THIS PAGE unclassified			

northern England and Wales (Shutts 1992; Shutts and Broad 1993; Vosper and Mobbs 1996) and during the Pyrenees Experiment (e.g. Satomura and Bougeault 1994; Broad 1996). Despite the successes of many of these recent studies, the capability of high-resolution models has not been fully evaluated for gravity-wave generation over three-dimensional complex topography such as the Alps.

The Mesoscale Alpine Programme (MAP) is a co-ordinated international endeavour to study mesoscale phenomena forced by three-dimensional topography in moist and dry environments, including gravity-wave generation and breaking (Bougeault *et al.* 2001). In preparation for the MAP field phase, a collaborative programme was established to evaluate the capability of high-resolution mesoscale numerical weather prediction models to predict the location and amplitude of gravity-wave launching and turbulent breakdown, in a series of experiments involving airflow over two-dimensional (Doyle *et al.* 2000) and three-dimensional (Doyle *et al.* 2002) topography. During the MAP field phase in autumn 1999, high-resolution numerical simulations were used as guidance for missions by research aircraft designed to observe mountain-wave breaking. One of the largest-amplitude gravity-wave events observed during MAP took place on 20 September 1999 over the Hohe Tauern range in the eastern Alps, and is the focal point of this study. It is noteworthy that in this case, and in a number of other situations during MAP, real-time mesoscale models forecasted vertically propagating large-amplitude waves rather than quasi-periodic partially trapped waves in the lee as were frequently observed (Bougeault *et al.* 2001).

Recent measurements from MAP and subsequent numerical model results suggest that processes that have received relatively little emphasis previously, such as in the boundary layer (e.g. Smith *et al.* 2002) and the effects of moisture, may be important for mountain-wave generation and propagation. One of the objectives of this study is to investigate the impact on mountain-wave dynamics of diabatic heating associated with precipitation upstream of a mountain crest. In one of the relatively few studies to consider effects of moisture on resonant lee waves, Durran and Klemp (1982) applied a two-dimensional model to examine the effects of latent-heat release on the wave dynamics for an atmosphere with a two-layer vertical structure. Changes to the moisture in the lowest layer were found to reduce the amplitude and untrap, or detune, the lee waves depending on the moisture profile. In some circumstances, changes to the moisture in the upper layer were found to amplify lee waves. Doyle and Shapiro (2000) noted that differential diabatic heating, associated with frontal-scale latent-heat release upstream of the central Norwegian mountains, resulted in a significant strengthening of a downslope 'windstorm' in the lee.

The lee-wave event that occurred over the Hohe Tauern range of the Alps on 20 September 1999 was observed *in situ* and by remote sensing instruments onboard the National Center for Atmospheric Research (NCAR) Electra. The primary objectives of this study are to: (i) document the lee-wave characteristics and dynamics through the use of the available observations and high-resolution numerical simulations; (ii) evaluate the capability of a high-resolution mesoscale model to simulate the gravity-wave characteristics; (iii) identify inadequacies that may limit accurate mesoscale predictions of topographically forced internal gravity waves; and (iv) explore the impact of diabatic processes associated with precipitation upstream of the Hohe Tauern crest on the lee-wave response. An observational overview of the lee waves is presented in section 2. The model description is contained in section 3. The nonlinear model results are described in section 4. The theoretical interpretation of the observations and nonlinear model simulations is discussed in section 5, followed by the summary and conclusions in section 6.

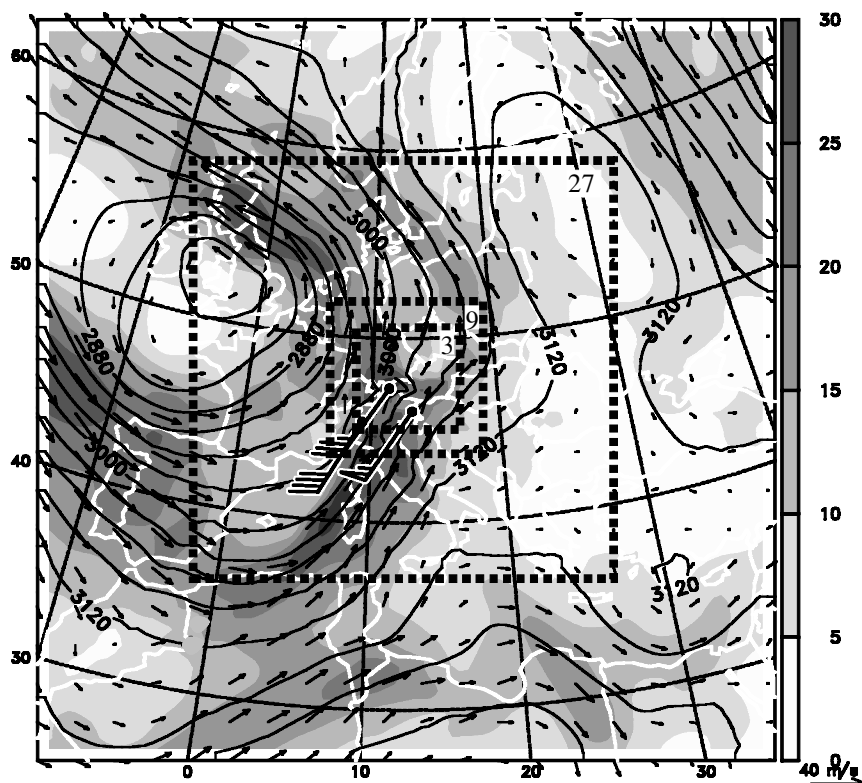


Figure 1. Wind speed and geopotential height analysis at 700 hPa valid at 1200 UTC 20 September 1999. The wind speed is shaded at 5 m s^{-1} intervals. The geopotential height contour interval is 30 m. Selected wind observations at 700 hPa are shown for Milan, Udine, and Innsbruck with one full wind barb representing 5 m s^{-1} and a pennant 25 m s^{-1} . The dotted boxes represent the domain locations of the first three grid meshes, with corresponding horizontal resolutions of 27, 9, and 3 km.

2. OBSERVATIONS OF THE LEE WAVES

(a) *Synoptic-scale overview*

A long-lived synoptic-scale system impacted the Alps during the period 17–21 September 1999, which corresponds to MAP Intensive Observing Period (IOP) 2, and created an environment favourable for the development of a number of topographically forced mesoscale phenomena such as föhn, gap flows, heavy precipitation, and gravity waves. Large-amplitude partially trapped gravity waves were observed on 20 September above the central portion of the Austrian Alps and are the primary mesoscale feature of interest in this study. The 700 hPa geopotential height and wind field analysis from the Naval Research Laboratory's Coupled Ocean/Atmosphere Mesoscale Prediction System (COAMPSTM) for 1200 UTC 20 September 2001, shown in Fig. 1, indicates that a south-south-westerly airstream was present over the Alps in advance of a large-scale trough associated with a 700 hPa closed cyclone over the United Kingdom. Several radiosonde observations located to the south and upstream of the Alps (e.g. at Milan and Udine, Italy) indicated 700 hPa wind speeds in excess of 20 m s^{-1} . The mean upstream wind speed between the surface and 3000 m as determined from the Verona, Udine and Milan, Italy, radiosondes at 1200 UTC 20 September was approximately 15 m s^{-1} , which implies significant potential for mountain-wave forcing.

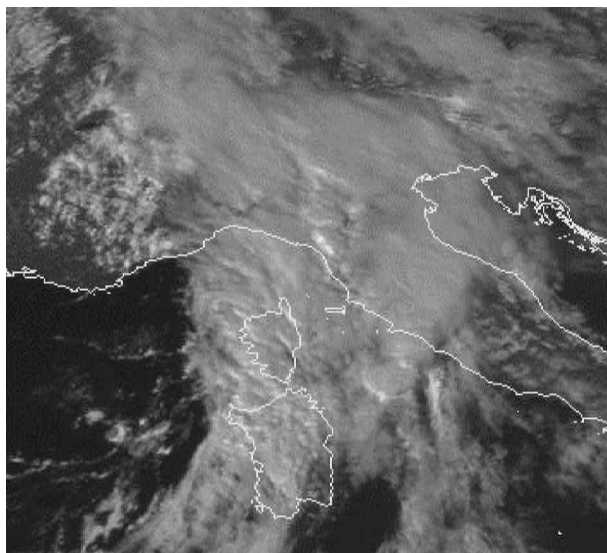


Figure 2. Visible image from Meteosat-6 rapid-scan data valid at 1345 UTC 20 September 1999.

A visible image from Meteosat-6 rapid-scan data for 1345 UTC 20 September, shown in Fig. 2, indicates a large area of clouds south of the Alps in a wide band extending from the central Mediterranean northwards through Italy and the Alps, which was linked with large-scale ascent associated with the synoptic-scale trough. A partial clearing in the cloud deck, or föhn window, indicative of strong orographic descent, is apparent just north of the Austrian Alpine crest with a series of lenticular clouds that have an along-cloud-axis orientation in an east–west direction parallel to the ridge crest and normal to the cross-mountain flow. Radar composites from this time period indicated the presence of an extensive shield of precipitation located to the south of the central Alpine crest, characterized by reflectivities of 30–40 dBZ with embedded regions of intense echoes exceeding 50 dBZ. Precipitation rates greater than 50 mm $(6\text{ h})^{-1}$ were observed upstream of the central and eastern Alpine crest (see Smith *et al.* 2003).

(b) Research aircraft observations

During MAP IOP 2 the NCAR Electra research aircraft, equipped with a suite of instrumentation including downlooking Scanning Aerosol Backscatter Lidar (SABL) and Global Positioning System (GPS) dropsondes, was used to observe the gravity-wave event over the Hohe Tauern range in the eastern Alps from 1150–1600 UTC 20 September 1999. The Hohe Tauern is an east–west oriented range that includes the highest peak in Austria, Grossglockner at 3797 m, and is one of the few quasi two-dimensional sections within the Alps. The aircraft flight track, shown in Fig. 3, consisted of a repeated series of six north–south segments oriented along the mean flow over Grossglockner at altitudes in the range 4900–6700 m. A series of quasi-periodic mountain waves were observed in the lee of Grossglockner by the suite of *in situ* and remote sensing instruments onboard the Electra. Additionally, mission scientists photographed numerous altocumulus lenticularis clouds from the aircraft. The lee-wave activity was observed during an extended period of deep south föhn and was particularly

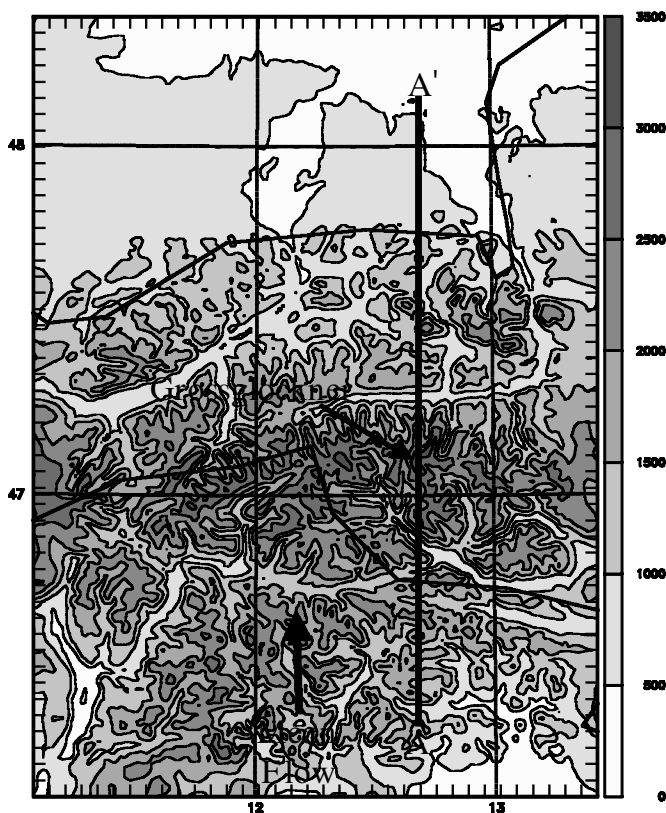


Figure 3. Topography (m) for the fourth grid mesh with horizontal resolution 1 km. AA' marks the aircraft flight path.

intense on 20 September, as indicated by the surface wind speed maximum of 50 m s^{-1} observed at Patscherkofel, Austria, near Innsbruck.

The atmospheric vertical structure in the vicinity of the Hohe Tauern was well observed because of the deployment of 13 GPS dropsondes from the research aircraft and the close proximity of several radiosonde observations at locations such as Verona and Innsbruck. Composite profiles have been constructed based on these dropsondes and radiosondes upstream and downstream of the Hohe Tauern crest. Upstream composite profiles, based on three dropsondes and the 1200 UTC Verona and Udine radiosonde ascents, are shown in Figs. 4(a)–(d). A two-layer structure of the static stability in the troposphere is present, as indicated by the potential-temperature composite profile (Fig. 4(a)). The layer between the surface and 6 km is characterized by a substantially larger static stability, corresponding to a Brunt–Väisälä frequency, N , of $\sim 0.013 \text{ s}^{-1}$, relative to the 6–12 km layer that has a mean N of $\sim 0.008 \text{ s}^{-1}$. This two-layer stratification is conducive for the development of trapped lee waves, as will be discussed in the following sections. The vertical wind shear is generally small above the crest of the Hohe Tauern (Fig. 4(b)). However, relatively weak low-level wind speeds from an easterly direction below 2.5 km are likely to be an indication of the presence of topographic blocking upstream of the Hohe Tauern (Fig. 4(c)), a phenomenon common to the Alps (e.g. Chen and Smith 1987). A wind direction that is nearly uniform at 210° above 2 km implies a lack of three-dimensional critical levels (e.g. Shutts 1998) in this

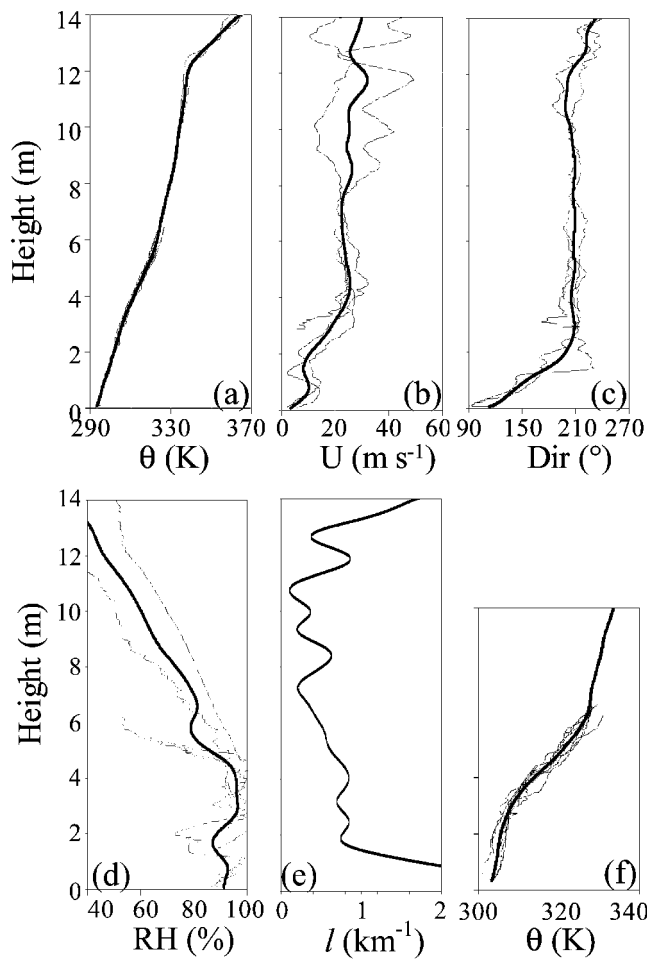


Figure 4. Profiles of: (a) potential temperature, (b) wind speed, (c) wind direction, and (d) relative humidity, all derived from upstream dropsondes and radiosondes for the period 1200–1500 UTC 20 September 1999. (e) The mean profile of the Scorer parameter based on these soundings. (f) Potential-temperature profiles based on soundings located downstream of Grossglockner in the wave region. Mean profiles are shown in black; individual dropsondes and radiosondes are shown in grey.

case. A mid-level moist layer is present below 5.5 km upstream of the Hohe Tauern (Fig. 4(d)).

Potential-temperature profiles were constructed of the region immediately downstream of the Hohe Tauern crest, in the area where the lee waves were observed, based on eight dropsondes and the Innsbruck radiosonde at 1200 UTC. The profiles indicate a three-layer structure to the tropospheric static stability, as shown in Fig. 4(f). Large static stability is present in the 3–6 km layer that contains a mean N of $\sim 0.014\text{ s}^{-1}$, with weaker static stability aloft and in the boundary layer below.

The six flight track segments of the research aircraft were aligned normal to the ridge axis, represented by segment AA' in Fig. 3, and were approximately along the mean cross-ridge-axis wind direction, which was from 210° . These flight segments were executed over Grossglockner at altitudes in the range 4900–6700 m, and consisted of varying lengths with the maximum being approximately 200 km. Occasional small

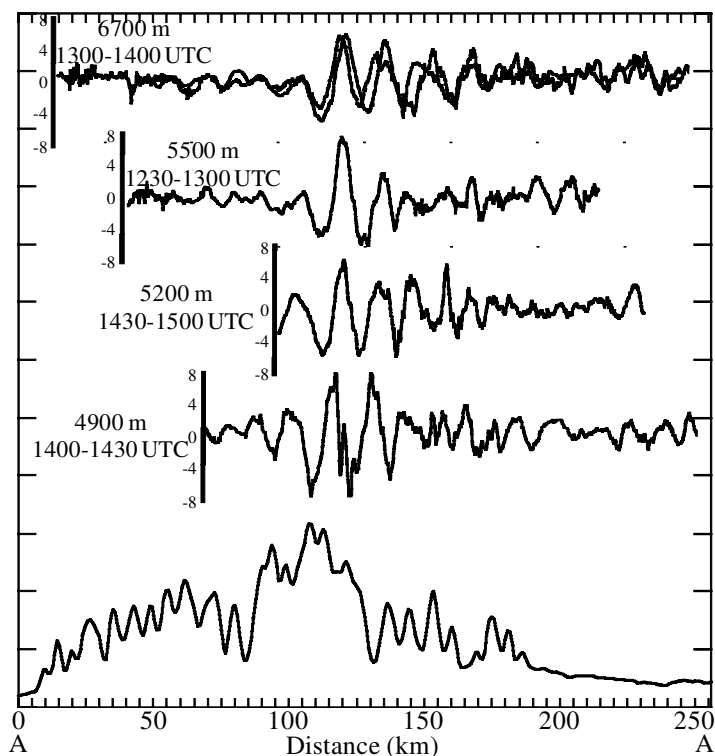


Figure 5. Vertical velocity (m s^{-1}) deduced from research aircraft observations over five legs at various altitudes on 20 September 1999. The topography along the flight track is shown along the abscissa.

deviations from AA' did occur during which the wave field was sampled above other portions of the Grossglockner topography. The derived vertical velocities from the aircraft measurements for five of the flight segments are shown in Fig. 5. The maximum vertical velocity magnitude is -9.3 m s^{-1} (downward) at 4900 m with a corresponding potential-temperature perturbation greater than 10 K. A total of four to seven distinct lee waves are apparent, with wavelengths of 10–13 km. Upstream of Grossglockner, relatively little wave activity is present in spite of the significant topography just upstream of the Hohe Tauern crest, once again an indication of upstream blocking (e.g. Smith *et al.* 2002). Lee-wave amplitudes are progressively damped and shorter in wavelength farther downstream of the most significant mountain waves. The cross-mountain wind component at the flight level is in the range $10\text{--}28 \text{ m s}^{-1}$, with the strongest winds immediately in the lee of Grossglockner at 4900 m and weakest upstream of the Alpine crest.

The backscatter coefficient from the downlooking SABL for the third flight segment at 1330–1400 UTC is shown in Fig. 6. Air-parcel vertical displacements (η) for five aircraft flight segments are also shown in Fig. 6, computed from the aircraft-derived vertical velocity (w) and horizontal velocity (U) through the application of the steady-state vertical displacement equation following Smith *et al.* (2002),

$$\eta(x) = \int_0^x (w/U) dx. \quad (1)$$

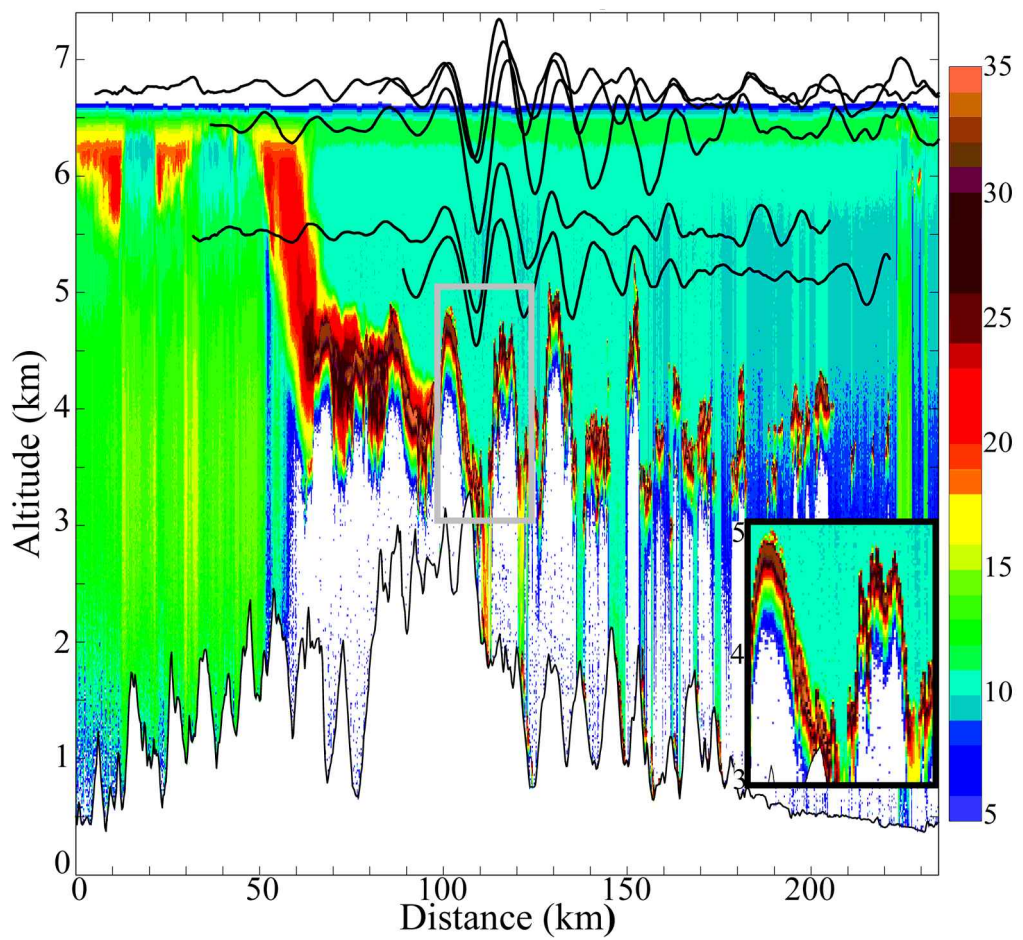


Figure 6. Backscatter coefficient from the Scanning Aerosol Backscatter Lidar (SABL) for the third flight segment at 1330–1400 UTC 20 September 1999. Air parcel displacements for five segments, derived from flight-level data and computed from Eq. (1), are shown in black. The inset in the lower right is an expansion of the SABL backscatter over Grossglockner in the 3–5 km layer corresponding to 1344–1350 UTC (denoted by the grey box in the main frame).

The integration is initiated at the upstream point of the flight segment and the mean vertical motion along the flight segment is removed. More than five lee waves are evident in the SABL backscatter data, and are generally coherent with the vertical parcel displacements. The most intense backscatter is apparently due to scattering by cloud liquid water in the wave crests. The existence of these lenticular clouds was confirmed visually by scientists on board the Electra and is in agreement with the Meteosat-6 rapid-scan data. The largest-amplitude lee-wave signature is located immediately downstream of the Alpine crest with a peak-to-trough vertical displacement of approximately 1.5 km at an altitude of 6500 m. The locations of the first several large-amplitude waves immediately in the lee of the crest appear to be quite steady at 6700 m and exhibit little vertical tilt. However, the smaller-amplitude waves farther downstream indicate considerable temporal variability and less vertical coherence. It is noteworthy that the lee waves are not in optimal phase with the topographic features beyond the Grossglockner crest, which is suggestive of a wave field that is decoupled

from the underlying topography. The inset in the lower-right portion of Fig. 6 is an expanded section of the SABL backscatter data for 1344–1350 UTC in the 3–5 km layer. A relatively smooth cloud layer, suggestive of laminar flow, descends immediately in the lee of the east–west mean ridgeline, and transforms into a cloud layer that contains high-frequency structures superimposed on the lee wave, possibly an indication of turbulent breakdown processes in the low-levels associated with Kelvin–Helmholtz instability (e.g. Smith 1991).

3. NONLINEAR NUMERICAL AND LINEAR ANALYTIC MODEL DESCRIPTIONS

(a) *Nonlinear numerical model*

The atmospheric portion of COAMPS (Hodur 1997) is applied for the nonlinear numerical simulations of idealized and observed flows in this study. The nonlinear model is a finite-difference approximation to the fully compressible, non-hydrostatic equations, and uses a terrain-following vertical coordinate transformation. In this application, the finite-difference schemes are of second-order accuracy in time and space. The compressible equations are integrated efficiently using a time-splitting technique through the use of a semi-implicit formulation for the vertical acoustic modes (Klemp and Wilhelmson 1978). The observed-flow simulations make use of the full suite of physical parametrizations to represent boundary-layer, radiative and moist processes including microphysical quantities (see Hodur 1997). The idealized simulations are adiabatic and make use of a free-slip lower boundary condition. The idealized simulations are performed without rotation, because the focus of these experiments is on the gravity-wave response forced by the relatively narrow Alpine ridge rather than on upstream blocking.

An incremental update data assimilation procedure that enables mesoscale phenomena to be retained in the analysis increment fields is used to initialize the real-data simulations. The initial fields for the model are created from multivariate optimum interpolation analyses of upper-air sounding, surface, commercial aircraft, and satellite data that are quality controlled and blended with the COAMPS 12 h forecast fields. The Navy Operational Global Analysis and Prediction System (NOGAPS) forecast fields are used for real-data lateral boundary conditions.

The domain configuration for the real-data simulations, as shown in Fig. 1, contains four horizontally nested grid meshes of 85×85 , 97×97 , 175×175 and 175×241 points, with horizontal grid increments (Δx) on the computational meshes of 27, 9, 3 and 1 km, respectively. The model contains 55 vertical levels on a non-uniform vertical grid; this consists of an increment of 10 m at the lowest level, gradually increases to 500 m at 7 km, and continues with 500 m increments to the model top at 22 km. A sponge layer of 5 km depth at the model top is used to mitigate spurious reflection of vertically propagating waves. The topographic data for the real-data simulations are based on the US Defense Mapping Agency (DMA) 100 m resolution dataset; this enables key topographic features, such as Grossglockner and the Hohe Tauern range, to be well represented on the innermost grid mesh, as shown in Fig. 3.

(b) *Linear analytic model*

A linear model is used to examine the mountain-wave dynamics in this case. The model solves the three-dimensional non-hydrostatic equations of linear mountain-wave theory for three vertical layers using the fast Fourier transform (FFT) method of Smith (1980) as extended by Smith (2001) and Smith (2002). The linearized equations for the horizontal velocity, vertical velocity, and pressure perturbation are reduced to a single

equation for the vertical displacement, $\eta(x, y, z)$. In this formulation, the dissipation of downward propagating waves due to critical-level absorption within the boundary layer can be represented by a reflection coefficient, q , of zero (see Smith 2001). A second free parameter of the linear model is the reference height, Z_{ref} , defined as the depth of the upstream stagnant or topographically blocked layer. The effective terrain height is then defined as $h(x, y) - Z_{\text{ref}}$, where $h(x, y)$ is based on the DMA 100 m resolution dataset. The terrain is reduced around the edges of the computational domain to avoid spurious wave wrapping associated with the FFT method. A Gaussian filter is used with an e-folding scale of 100 km, and is centred on the Alpine crest so that the Hohe Tauern range is realistically represented.

4. NONLINEAR NUMERICAL SIMULATIONS

A 24 h model integration, initialized at 0000 UTC 20 September 1999, was performed using COAMPS with a horizontal resolution of 1 km on the fourth and finest grid mesh. In the 1200–1500 UTC (12–15 h) time period*, the model develops a series of well-defined lee waves in agreement with the timing suggested by Meteosat-6 rapid-scan visible satellite imagery available with a time resolution of 5 minutes and a 3 km pixel size. The horizontal and vertical velocities on the 1 km mesh at 4.9 km, which was the height at which the research aircraft indicated the maximum lee-wave amplitude, is shown in Fig. 7 for 1400 UTC 20 September. A complex banded vertical velocity pattern is apparent in the lee of the Hohe Tauern crest, with a dominant wavelength of approximately 15 km. The bands in the vertical velocity field are oriented in an east–west manner similar to the rapid-scan imagery (Fig. 2), and contain significant along-band variations. The vertical velocities at 4900 m are in the range $+15.3$ to -13.6 m s^{-1} , with the largest amplitude associated with the first wave crest in the lee of the Hohe Tauern.

A vertical cross-section of potential temperature and vertical velocity valid at 1400 UTC (14 h) 20 September, constructed along the BB' line segment (Fig. 7) parallel to the aircraft flight path and through the lee-wave train, is shown in Fig. 8(a). The tropospheric static stability is composed of two layers: one between the surface and 6 km characterized by a mean N of 0.013 s^{-1} , and an upper layer between 6 and 10.5 km with weaker stability and a mean N of 0.008 s^{-1} , in agreement with the dropsonde composites discussed previously. The flow upstream of the Hohe Tauern is decoupled from the topography below due to blocking in advance of the airstream passing over Grossglockner, and subsequently a series of approximately six large-amplitude lee waves forms downstream of the crest. The vertical velocity and potential-temperature perturbations associated with the lee waves are in quadrature, as exhibited by the isentropic crests and troughs that are nearly coincident with the zero vertical velocity contour, which is a characteristic of internal gravity waves (e.g. see Smith 1979). The gravity-wave phase-tilt lines deduced from the potential-temperature and vertical velocity fields are nearly vertical in the lower troposphere, which is an indication that the internal gravity-wave energy is channelled into, or trapped in, a horizontal waveguide that limits vertical propagation. Waves with longer horizontal wavelengths that are forced by the larger-scale components of the topography propagate vertically into the stratosphere and break in the 12–13 km layer over Grossglockner, similar in character to other lee-wave events (Shutts 1992; Shutts and Broad 1993; Lane *et al.* 2000).

* Equivalence between actual times UTC and model times as hours into the integration applies throughout this paper, and is not repeated hereafter.

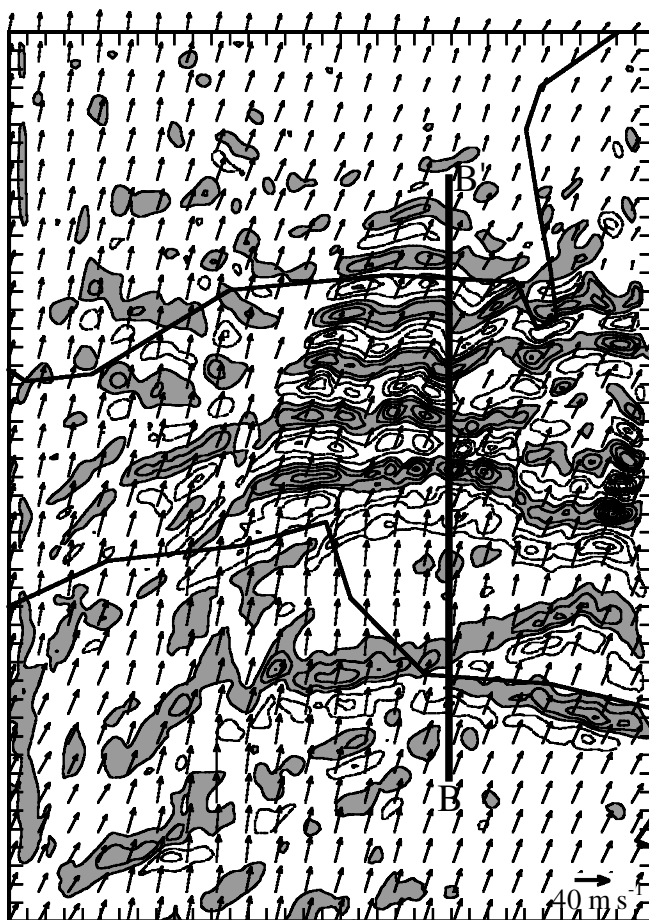


Figure 7. Simulated vertical velocity (m s^{-1}) at 4900 m for the fourth grid mesh, with horizontal resolution 1 km, valid at 1400 UTC 20 September 1999. The contour interval is 1 m s^{-1} with upward vertical velocities greater than 1 m s^{-1} shaded in grey. The horizontal wind speed at 4900 m is represented by the wind vectors and plotted every eight grid points, with a reference vector in the lower right-hand corner. Tick marks along the boundary are plotted every 5 km. Line BB' denotes the approximate flight path and the location of a vertical cross-section (see Fig. 8). The international borders are denoted by the bold lines.

A large region of precipitation was present during IOP 2 upstream of the Hohe Tauern associated with synoptic-scale and topographically forced ascent (see Smith *et al.* 2003). Diabatic heating associated with precipitation upstream of the crest may have been substantial enough to influence the lee-wave development through the modulation of the upstream stratification as previously discussed in Doyle and Shapiro (2000). In order to explore this hypothesis further, a three-dimensional numerical simulation was performed using the nonlinear COAMPS that excludes latent-heat release and cloud microphysical processes, including interaction with radiation; this is referred to hereafter as the 'dry simulation'.

A vertical cross-section of potential temperature and vertical velocity from the dry simulation constructed along the BB' segment (Fig. 7) valid at 1400 UTC 20 September (14 h) is shown in Fig. 8(b). The mid- and upper-tropospheric static stability is increased significantly, and additionally the low-level stability is decreased slightly relative to the control (i.e. full physics) experiment (Fig. 8(a)). The latent heating and

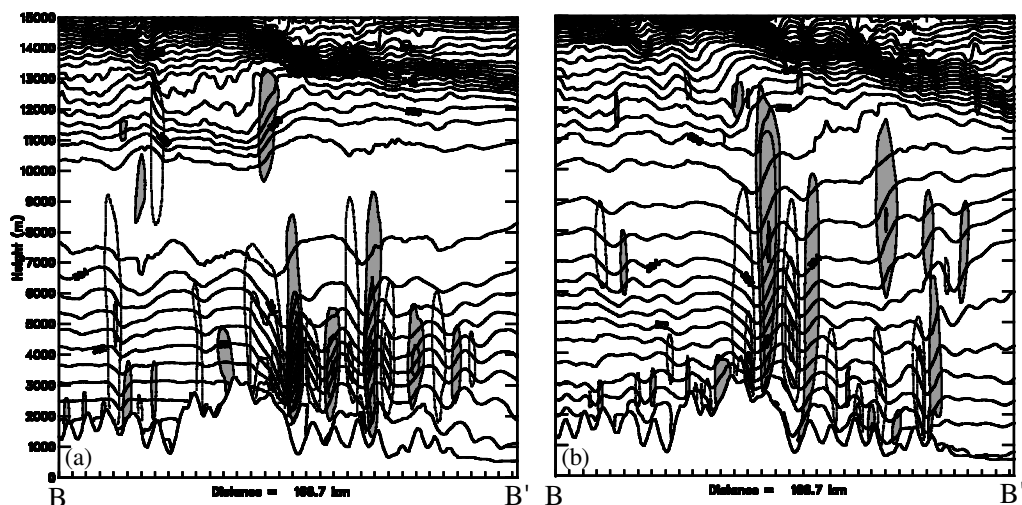


Figure 8. Vertical cross-section of potential temperature (K) and vertical velocity (m s^{-1}) along BB' (see Fig. 7) valid at 1400 UTC 20 September 1999 for: (a) the control simulation, and (b) the simulations with no latent-heat release. Potential temperature is contoured every 3 K, and vertical velocity every 2 m s^{-1} with upward vertical velocities greater than 2 m s^{-1} shaded in grey. Tick marks along the abscissa are plotted every 5 km.

evaporation associated with cloud and precipitation processes leads to destabilization in the 7–10.5 km layer and net warming in the layer between the surface and 7 km upstream of the crest during the first 14 h of the simulation. Trajectory analysis using the second nested grid mesh ($\Delta x = 9 \text{ km}$) of the control simulation, indicates that parcels residing near the top of the wave duct within the weak-stability layer aloft have a source region south of the Hohe Tauern in the mid-troposphere within the precipitating region. The modelling results of Smith *et al.* (2003) also suggest that evaporation of snow in the mid-troposphere may contribute to cooling and further destabilization. The results have some similarities with a case considered by Durran and Klemp (1982), in which mid-level moisture was introduced which resulted in the amplification of weak dry waves through the reduction in the height of the wave-trapping interface. However, in the case considered here nearly all of the latent heat is applied upstream of the crest, while the largest flow differences are present in the downstream plunge and lee-wave response. The results suggest that the most significant aspect of the latent-heat release is the modification of the environment, rather than acting locally in the plunging flow and lee waves.

A direct comparison of vertical velocities measured by aircraft with the simulated vertical velocities for the inner grid mesh ($\Delta x = 1 \text{ km}$) from the full-physics simulation is shown in Figs. 9(a)–(f). Simulated values are interpolated to the aircraft GPS locations at a resolution of 1 Hz for the six flight paths of the research aircraft. The model topography for the 1 km grid mesh, shown at the bottom of Fig. 9, compares well with the 100 m resolution topography (not shown), which indicates that the crucial topographic features are well resolved. Overall, the vertical velocities predicted by the model agree quite well with measurements from the research aircraft. In particular, the maximum magnitude of the vertical velocity for each aircraft leg is simulated accurately. For example, the maximum simulated vertical velocity for all aircraft legs is 10.5 m s^{-1} and is located at 4900 m (Fig. 9(d)). This simulated value agrees well with the maximum magnitude of the observed vertical velocity of 9.3 m s^{-1} , and is located at the same

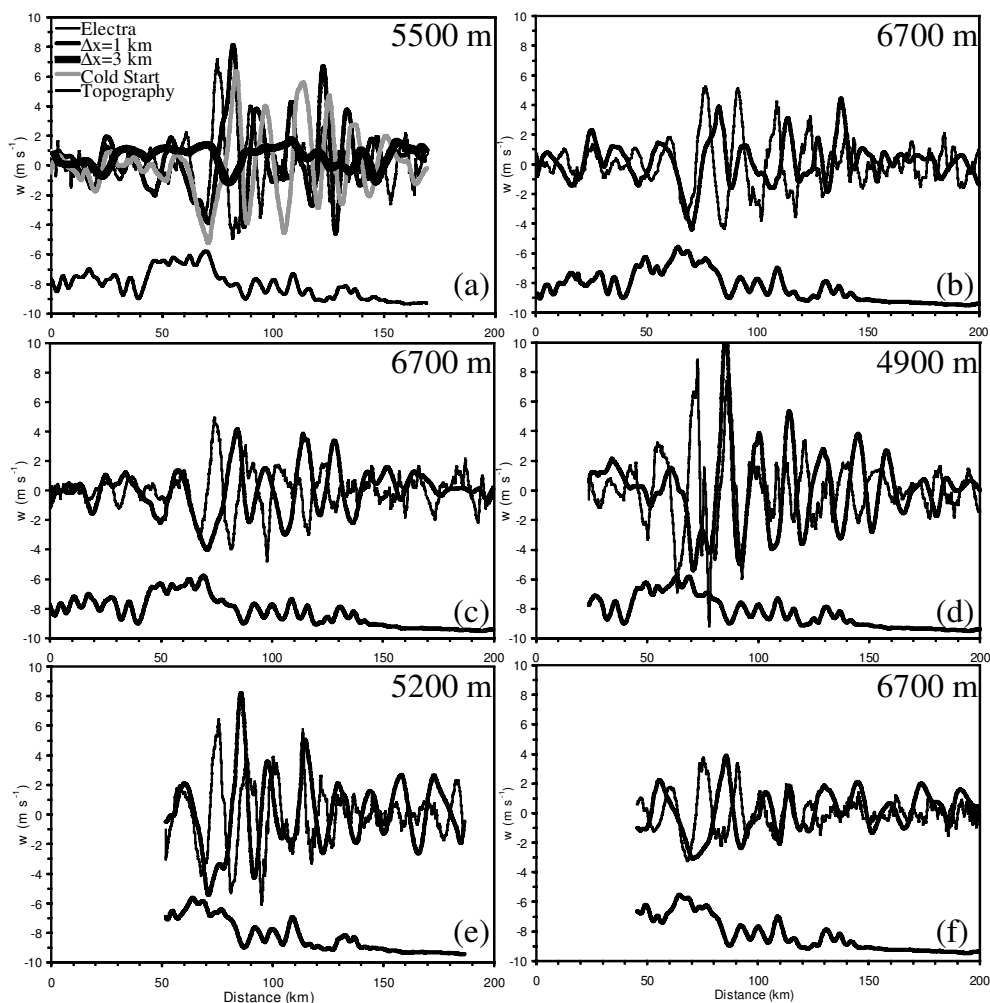


Figure 9. Vertical velocity (m s^{-1}) from the Electra aircraft (thin lines) and from the fourth grid mesh, with horizontal resolution 1 km, interpolated to the aircraft positions (bold lines) at: (a) 1234–1258 UTC 20 September 1999 and 5500 m, (b) 1300–1324 UTC and 6700 m, (c) 1330–1400 UTC and 6700 m, (d) 1408–1427 UTC and 4900 m, (e) 1435–1454 UTC and 5200 m, and (f) 1504–1527 UTC and 6700 m. Vertical velocities from a cold start initialization experiment and the third mesh with horizontal resolution 3 km are also shown in (a). The model terrain for the 1 km mesh interpolated to the aircraft position is shown along the abscissa.

altitude. The simulation captures many of the observed lee-wave characteristics, such as the dominant wavelength of approximately 15 km and the maximum amplitude response in the first wave in the lee of the crest with subsequent waves damped with distance downstream of Grossglockner. The model accurately simulates the reduction in the lee-wave amplitude at 6700 m from the 5 m s^{-1} maximum observed during the 1300–1400 UTC time period (Figs. 9(b)–(c)) to the $3\text{--}4 \text{ m s}^{-1}$ maximum at 1500 UTC. However, a noticeable shortcoming of the simulation is that the wavelength of the primary lee wave is too long relative to the aircraft observations. The results from an additional COAMPS simulation that used a horizontal grid increment of 0.5 km, indicate that the wavelength discrepancy is not particularly sensitive to increased horizontal resolution. The model simulation that uses a NOGAPS analysis at 0000 UTC 20 September as the first-guess

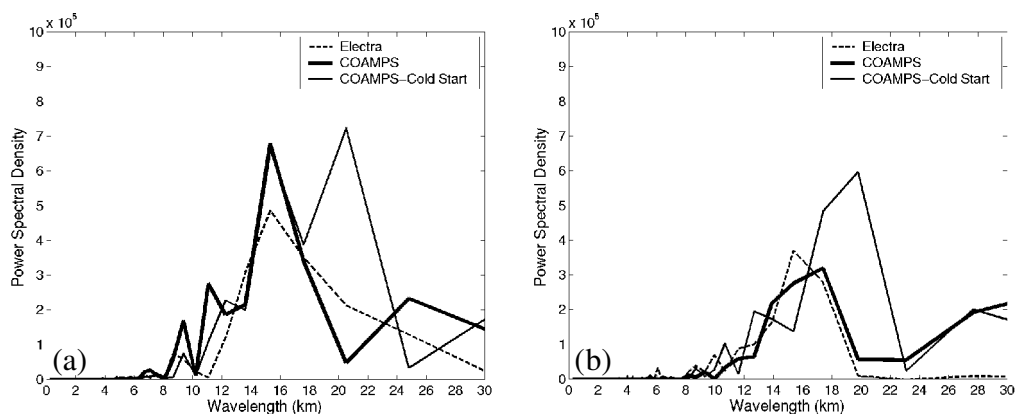


Figure 10. Power spectral density ($\times 10^5 \text{ m}^2 \text{ s}^{-2}$) of the vertical velocity as a function of wavelength for the Electra aircraft, from the fourth grid mesh with horizontal resolution 1 km with data assimilation, and from the simulation with a cold start initialization for the legs at: (a) 5500 m (1234–1258 UTC 20 September 1999) and (b) 6700 m (1330–1400 UTC).

field (referred to here as a ‘cold start’) in contrast to the control simulation that uses an incremental data assimilation procedure, contains an even larger wavelength error (Fig. 9(a)) indicating that the lee-wave characteristics are sensitive to relatively small changes in the initial and upstream conditions. It should also be noted that the lee waves are of sufficiently short wavelength (~ 12 – 15 km) such that the 3 km grid mesh is not capable of resolving the lee waves, as indicated in Fig. 9(a).

In order to compare further the simulations with the observations in a quantitative manner, the vertical velocity power spectral density is computed for: the research aircraft data, the COAMPS simulation from the fourth grid mesh ($\Delta x = 1$ km), and an identical simulation that makes use of no mesoscale data assimilation at the initial time (0000 UTC 20 September). The model-simulated vertical velocity is interpolated to the aircraft locations at a 1 Hz frequency. The mean is removed from the observed and simulated vertical velocities and the data are linearly detrended. The power spectral density for the first (1234–1258 UTC at 5500 m) and third (1330–1400 UTC at 6700 m) aircraft legs are shown in Fig. 10. The simulated and observed power spectral densities are in reasonable agreement for the 5500 m leg, as exhibited by the dominant wavelength of approximately 15 km (Fig. 10(a)). The power spectrum for the 6700 m leg (Fig. 10(b)) indicates a simulated primary wavelength of 17 km compared with the 15 km observed wavelength. The power spectral density for the cold-start model simulation contains some deficiencies, including too much energy in the longer wavelengths (Fig. 10(a)) and a resonant wavelength that is larger than that observed (Fig. 10(b)). Both simulations use identical terrain representations, which implies that the power spectra differences in Fig. 10 must be due to changes in the upstream profile. The mesoscale data assimilation used in this study provides a more accurate representation of the upstream conditions, which leads directly to a more realistic simulation of the primary wave and lee-wave train as indicated by the vertical velocity (e.g. Fig. 9(a)) and power spectra (Fig. 10).

5. THEORETICAL INTERPRETATION

The mountain-wave response to flow over the Hohe Tauern in this case is quite complex due to a number of factors including latent-heat effects, the plunge of the airstream immediately in the lee of the crest, and the subsequent generation of trapped

lee waves. The latent-heat effects occur primarily upstream of the crest, yet the fundamental flow differences between the simulations with and without latent-heat release (Fig. 8) are greatest in the downstream plunge and lee waves. This implies that the significance of the latent-heat release may be in the modification of the environment rather than action locally in the lee-wave crests. Thus, the dynamical issues are sufficiently complicated and interrelated to warrant several different approaches to aid the theoretical interpretation of the observations and nonlinear numerical model simulations. The results from four different types of fundamental analysis tools based on theoretical approaches are discussed in the following section. Eigenvalue solutions to the linear vertical structure equation are used to compute resonant wavelengths of the lee waves. Three-layer linear analytic solutions are obtained to provide insight into the significance of the weak-stability layer aloft that arises from the latent-heat release upstream of the crest. Idealized nonlinear numerical model simulations are used to further elucidate the dependence of the gravity-wave response on the vertical distribution of upstream latent heating. Lastly, the nonlinear theory of Smith (1985) is applied to understand the dynamical response in the downstream plunge.

(a) Eigenvalue solutions

Linear theory is used to explore the significance of the vertical variations of the observed and simulated static stability and winds. The vertical amplitude of a single plane harmonic wave is principally governed by the vertical structure equation, here applied in two dimensions,

$$\frac{d^2 \hat{w}}{dz^2} + (l^2 - k^2) \hat{w} = 0, \quad (2)$$

where $\hat{w}(z, k)$ is the transformed vertical velocity, k is the horizontal wave number and l is the Scorer parameter,

$$l^2(z) = \frac{N^2}{U^2} - \frac{1}{U} \frac{\partial^2 U}{\partial z^2}, \quad (3)$$

where $U(z)$ is the cross mountain wind speed and z is the vertical coordinate. Resonant lee waves will develop if l decreases rapidly with height (e.g. Scorer 1949). The profile of the Scorer parameter is computed based on smoothed mean profiles of cross-mountain wind speed and potential temperature from the Verona and Udine soundings and three dropsondes upstream of the Hohe Tauern (Figs. 4(a)–(c)), and is shown in Fig. 4(e). Above the mountain crest the shear is relatively small in this case, and the Scorer parameter profile is dominated by vertical stability variations (Fig. 4(a)–(c)). Although the upstream profiles indicate nearly saturated conditions in the lower troposphere (Fig. 4(d)), descent in the lee of the Hohe Tauern results in a sub-saturated lee-side mean state with only localized saturated regions corresponding to the lee-wave crests. Thus, computation of a Scorer parameter with a saturated mean state would not be suitable, and it follows that to a first approximation l can be computed based on dry conditions. The profile indicates a decrease of l with height in the 2.5–7 km layer that is sufficient to support the development of partially trapped lee waves. Above 13 km, the l profile once again increases, in part due to the large N in the stratosphere.

Upstream profiles of potential temperature, cross-mountain wind speed and Scorer parameter from COAMPS valid at 1400 UTC 20 September were calculated for a 25 km² box centred 65 km south of Grossglockner. These profiles are shown in Fig. 11. The profiles exhibit many characteristics similar to the composite sounding based on the dropsondes and radiosondes (Fig. 4) such as: the large static stable layer in the

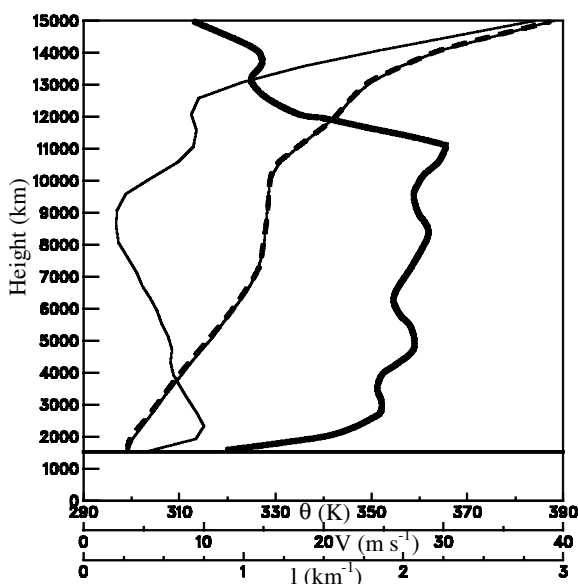


Figure 11. Simulated mean profiles of potential temperature (K, dashed line), cross-mountain wind component (m s^{-1} , bold line), and Scorer parameter (km^{-1} , thin solid line) for a 25 km^2 box centred at 65 km south of Grossglockner valid at 1400 UTC 20 September 1999.

lower troposphere ($N \sim 0.013 \text{ s}^{-1}$) capped by weak stability in the 7–10.5 km layer ($N \sim 0.007 \text{ s}^{-1}$), slightly less than that observed; wind speeds in excess of 20 m s^{-1} at 3500 m at the Hohe Tauern crest; and relatively weak vertical shear through the troposphere above the crest. The decrease with altitude of the Scorer parameter in the troposphere can be primarily attributed to the weak-stability layer aloft. The reverse vertical shear of the cross-mountain wind component and large N above 11 km lead to a significant increase in the Scorer parameter in the lower stratosphere, similar to calculations based on the observed profiles. The waves are no longer trapped in the lower stratosphere, leading to vertical propagation and steepening consistent with Fig. 8(a).

The dominant resonant wavelength is calculated based on linear theory using the Scorer profiles derived from the radiosonde and dropsonde observations and the model simulation. Equation (2) is solved repeatedly for a range of wave numbers following Shutts and Broad (1993) using Gaussian elimination. A radiation condition is used at the upper boundary, and the surface amplitude is arbitrarily set to unity. Application of the Scorer parameter profile based on the dropsonde and radiosonde observations (Fig. 4(e)) yields a maximum amplitude response for a horizontal wavelength of 13.2 km, which is in reasonable agreement with the observed horizontal wavelength of 15 km (Fig. 10). The solution to (2) using the Scorer parameter profile computed from the model simulation valid at 1400 UTC 20 September (Fig. 11) results in a dominant resonant horizontal wavelength of 17.4 km, that is slightly longer than that observed, which is consistent with the relative differences between the power spectral density calculations for the observed and simulated conditions (Fig. 10).

(b) Linear analytic solutions in three dimensions

In order to further quantify the implications of variations of mean state stratification in the vertical, three-dimensional linear analytic solutions were obtained for the lee waves over the Hohe Tauern following Smith *et al.* (2002). This formulation of the

TABLE 1. IDEALIZED THREE-LAYER MEAN STATE PARAMETERS FOR THE LINEAR ANALYTIC SOLUTIONS

Layer	Speed (m s ⁻¹)	Direction	N (s ⁻¹)		l (m ⁻¹)		Altitude (km)
1	20	180	0.013	0.013	6.5×10^{-4}	6.5×10^{-4}	2–7
2	25	180	0.008	0.013	3.2×10^{-4}	5.2×10^{-4}	7–11
3	10	180	0.02	0.02	2.0×10^{-3}	2.0×10^{-3}	>11

The second values given for each Brunt–Väisälä frequency, N , and Scorer parameter, l , correspond to a second linear calculation that features constant stability in the lowest two layers.

mountain-wave linear theory utilizes two free parameters, Z_{ref} and q the reflection coefficient, in addition to the three-layer mean state structure shown in Table 1, which is based on the observed upstream profiles (Fig. 4). The choice of an upper-level wind speed of 10 m s⁻¹ is based on the nonlinear numerical simulations as well as the soundings in close proximity to the wave region (e.g. Munich). The bottom level for the linear calculations is chosen to be 2000 m and corresponds to the depth of the upstream blocking, as indicated by the weak flow and the prevalence of an easterly wind component in the low levels of the observed profiles (Fig. 4). The *in situ* vertical velocity (Fig. 5), backscatter from the SABL (Fig. 6), and derived vertical parcel displacements (Fig. 6) indicate that the airflow in the 4–7 km layer is decoupled from the topography upstream of the Hohe Tauern crest, which is consistent with the presence of the upstream blocking and provides further support for the selection of Z_{ref} . A value of 0.9 is chosen for q , based on the observational and nonlinear model results that indicate downward propagating waves are reflected at or near the lower boundary, rather than absorbed in a surface-based critical layer such as in the case of gravity waves forced by Mont Blanc described by Smith *et al.* (2002). In this application, q is selected to be 0.9 rather than unity to prevent spurious wrapping of the wave-field solution in the finite domain due to the Fourier solution method. The solution in the interior of the domain using $q = 0.9$ is nearly identical to the calculation using $q = 1.0$.

The parcel displacements are computed from the linear analytic solutions following Smith *et al.* (2002). A grid comprised of 1024×1024 points spaced 1 km apart is used. The size of the grid mesh is sufficiently large for the periodic boundary conditions not to influence the solution on the interior of the grid mesh. The non-Boussinesq effects are represented in the parcel displacement calculations by the coefficient $\exp(z/2H)$, where H is the density-scale height.

The non-hydrostatic linear solution contains the salient characteristics of the observed and nonlinear simulated flow. A vertical cross-section of the parcel displacements heights using linear theory is shown in Fig. 12(a) for the three-layer mean state (Table 1). The cross-section is oriented along the mean flow and research aircraft transect. A series of trapped lee waves is present between the surface and 7 km, located downstream of Grossglockner. The first four waves in the lee of the crest are largest in amplitude, and they subsequently decay downstream similar to the observations (Figs. 5–6) and nonlinear simulation (Fig. 8(a)) of the lee-wave train. The dominant horizontal wavelength of the lee waves is approximately 15 km, similar to the observed wavelength (Fig. 10). However, the maximum parcel vertical displacement is 1 km, which is less than the maximum of 1.5 km based on the research aircraft data (Fig. 6). Gravity waves with wavelengths longer than the critical horizontal wavelength, $\lambda_c = 2\pi/l$, are able to propagate vertically through the wave duct; in this case gravity waves with $\lambda > 20$ km can propagate through the first two layers. The substantial increase of the mean state Scorer parameter above 11 km (Table 1) enables the waves to propagate vertically with an increased amplitude due to non-Boussinesq effects.

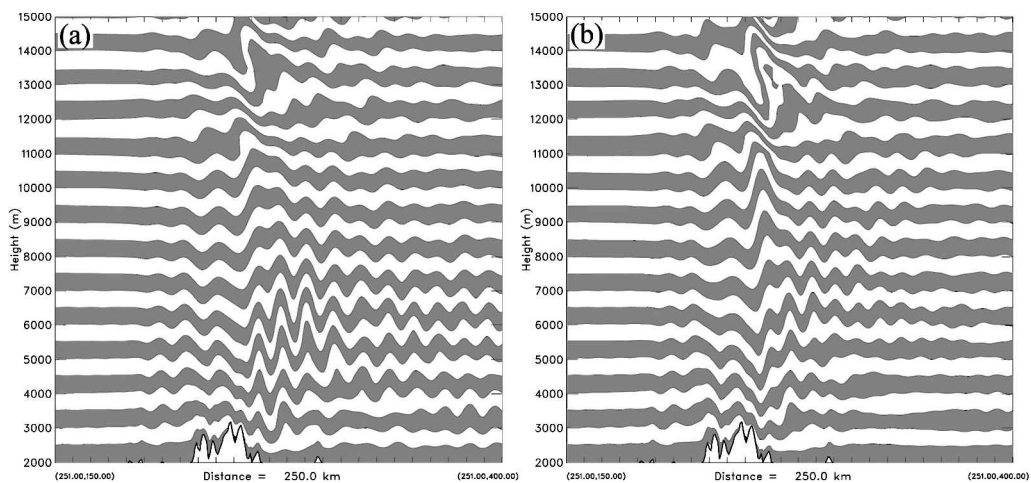


Figure 12. Vertical cross-section of the parcel displacement field from linear analytic solutions for a mean state (a) based on observed profiles and (b) with the upper-tropospheric weak-stability layer removed. Tick marks along the abscissa are plotted every 10 km.

An additional non-hydrostatic linear analytic solution was obtained for a mean state with $N = 0.013 \text{ s}^{-1}$ in the lowest two layers, which implies that l decreases less rapidly with height (Table 1). This altered state is intended to test the effect of upstream latent heating. A vertical cross-section of the parcel vertical displacements for this calculation is shown in Fig. 12(b). Although a portion of the wave energy remains trapped due to the vertical shear in the lowest two layers, the amplitudes of the lee waves are reduced considerably. The increased Scorer parameter in the second layer results in a decrease in λ_c to 9.6 km and greater energy in vertically propagating modes, in contrast to the solution that used $N = 0.008 \text{ s}^{-1}$ in the second layer (Fig. 12(a)). The increase in vertically propagating wave energy leads to larger-amplitude waves in the upper levels with wave steepening apparent in the 12–14 km layer (Fig. 12(b)).

(c) Idealized nonlinear numerical simulations

The net heating associated with the precipitation is estimated assuming steady flow using:

$$\Delta T = \frac{PL}{FC_p}, \quad (4)$$

where P is the precipitation in the period 0600–1200 UTC 20 September, F is the air mass flux, L is the latent heat of condensation, and C_p is the specific heat at constant pressure. The computation follows the methodology of Smith *et al.* (2003), is performed for a box centred on the Hohe Tauern bounded by 11–13°E and 45.5–48°N and extends up to 5 km. The simulated precipitation for this time period is in good agreement with observed values deduced from the high-density rain-gauge network, which indicated rates in excess of 50 mm (6 h)^{-1} upstream of the Alpine crest during the period 0600–1200 UTC. The estimated heating associated with precipitation, using the model results of Smith *et al.* (2003) and obtained through the application of (4), is 3.1 K.

The airflow over Grossglockner has a tendency to generate more vertically propagating waves and exhibit less of a trapped-wave response in the dry simulation (Fig. 8(b)), than in the control simulation (Fig. 8(a)). The cross-mountain winds are

slightly stronger in the simulation without latent-heat release than in the control. For example, an upstream profile averaged over the same 25 km^2 area as the control profile (Fig. 11) indicates a cross-mountain wind speed just above the mountain crest at 4 km of 27 m s^{-1} , in contrast to the 24 m s^{-1} of the control simulation. The low-level vertical shear is slightly larger in the dry simulation; however, the N^2/U^2 term in (3) dominates the curvature term in the Scorer parameter calculation for both the control and dry simulations. The two simulations have similar upstream Scorer profiles in the 3–7 km layer. The largest difference between the two simulated profiles occurs in the 7–10 km layer, where the stratification is larger in the dry simulation. It follows that the Scorer profile decrease is less rapid in the vertical in the dry simulation and, as a result, the wave duct is considerably weakened and the mean state is not as conducive for trapped waves. The primary wave has a vertical velocity maximum that extends through the depth of the troposphere in the dry simulation, which is suggestive of greater energy in vertically propagating modes. These results highlight the importance of the weak-stability layer aloft for wave trapping and are in qualitative agreement with the linear analytic solution results (Fig. 12).

In order to gain a greater understanding of the role of latent-heat release in modulating the gravity-wave response, a series of simplified numerical experiments were performed using COAMPS. The model is initialized with a horizontally homogeneous uniform basic state with $N = 0.013 \text{ s}^{-1}$ and $U = 20 \text{ m s}^{-1}$ that is hydrostatically balanced. The topography is specified using a Witch of Agnesi profile:

$$h(x) = \frac{h_0 a^2}{x^2 + a^2}, \quad (5)$$

for a two-dimensional mountain of height $h_0 = 800 \text{ m}$, and half-width $a = 10 \text{ km}$. The model is applied in a two-dimensional configuration with no moist or radiative processes. The turbulent vertical fluxes of horizontal momentum are set to zero at the lower boundary. The horizontal grid increment is 1 km and the vertical grid increment is 200 m with a model top at 12.8 km. The lateral boundaries make use of a radiation condition. At the model top, a radiation boundary condition is used to mitigate the reflection of waves following Klemp and Durran (1983) and Bougeault (1983). The computational domain is 300 km in length.

In these experiments, a simplified heating tendency profile is specified as:

$$\frac{\partial \theta_h}{\partial t} = \dot{\theta}_m \sin \left\{ \pi \frac{(z - z_b)}{z_t - z_b} \right\}, \quad (6)$$

where θ_h is the potential-temperature perturbation due to the specified heating, z_b and z_t are the heights above the surface of the bottom and top of the heating profile, respectively. The maximum heating rate, $\dot{\theta}_m$, is specified as 1.5 K h^{-1} at the centre of the profile, which is in general agreement with heating rates associated with convection (e.g. Kuo and Anthes 1984; Ogura 1984). The heating profile (6) is applied to all grid points upstream of the mountain crest and is invariant with time. The heating profile is not necessarily intended to replicate the effects of the precipitation during IOP 2 or any specific case. The simple heating profile is used to explore the potential impact on mountain-wave generation due to latent-heat release upstream. For simplicity evaporation is ignored, although it may be important for further reduction in the static stability in the mid-troposphere present in the observed profiles (Fig. 4) and numerical simulation (Smith *et al.* 2003).

The potential temperature and vertical velocity at the 9 h integration time for four experiments are shown in Fig. 13. The static stability and wind speed chosen for these

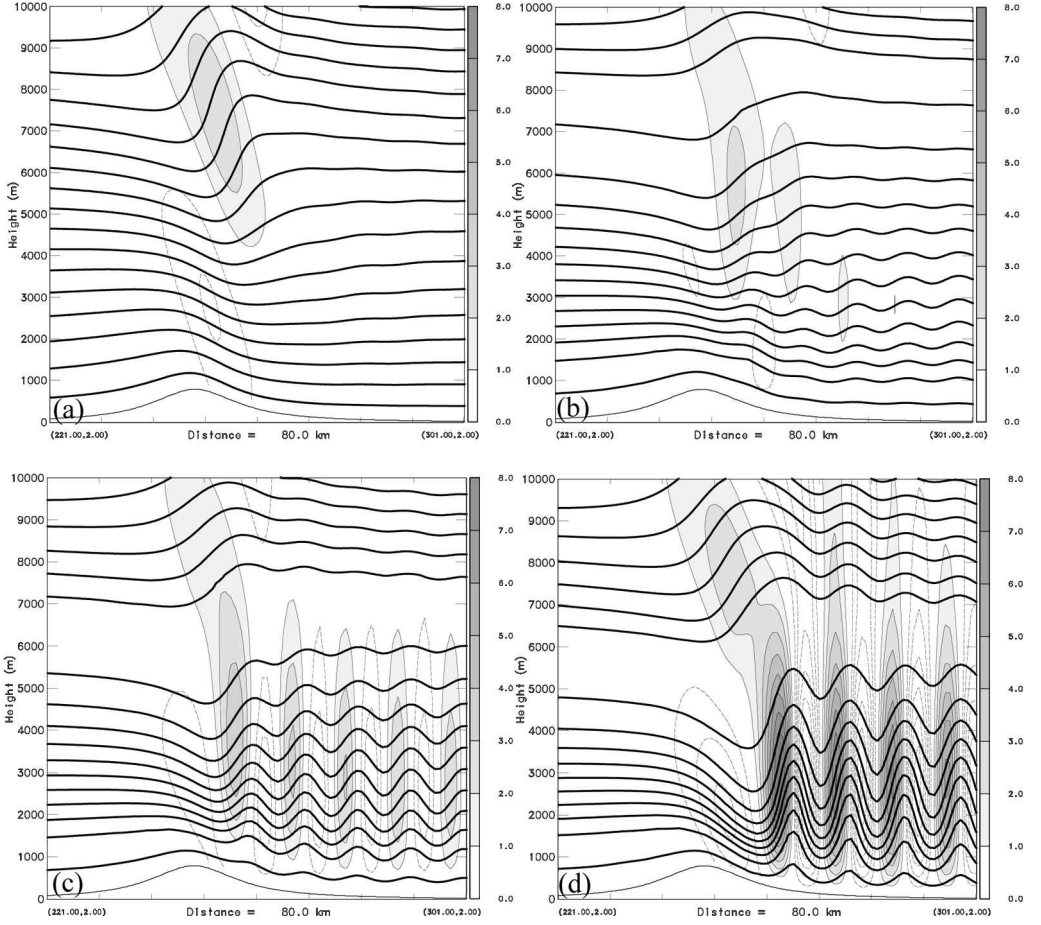


Figure 13. Potential temperature (K, bold lines, contour interval 3 K) and vertical velocity (m s^{-1} , contour interval 1 m s^{-1}) after 9 h for two-dimensional simulations: (a) without any heating; (b) with a constant heating profile with base 1 km and top at 8 km; (c) as (b) but top at 7 km; and (d) as (b) but top at 6 km. Upward velocities greater than 1 m s^{-1} are shaded (see keys) and downward contours are dashed. Tick marks along the abscissa are plotted every 10 km.

experiments are similar to the observed mean conditions in the lower troposphere and identical to the lowest-layer parameters for the linear solutions. The simulation without heating in the upstream exhibits a hydrostatic wave response with a classic upstream phase tilt to the gravity waves (Fig. 13(a); e.g. Smith 1979).

Several additional experiments were performed to explore the sensitivity to the depth of the heating. The base of the heating profile in these experiments is constant at 1 km above the surface. Above $(z_t - z_b)/2$, the static stability decreases, in contrast to below the mid-level of the heating profile where it increases. The wave response changes markedly as z_t and the height of the wave duct is reduced. The Scorer parameter (N/U) decreases with height because the imposed heating profile is sufficient to support trapped waves for cases where $z_t = 8, 7$ and 6 km, as indicated in Figs. 13(b)–(d). However, for the case with $z_t = 6$ km (Fig. 13(d)) the wave amplitude increases substantially, with a maximum vertical velocity of 9.4 m s^{-1} compared to 3.4 m s^{-1} for $z_t = 7$ km (Fig. 13(c)). The maximum horizontal wind speed increases by 25% when z_t is reduced

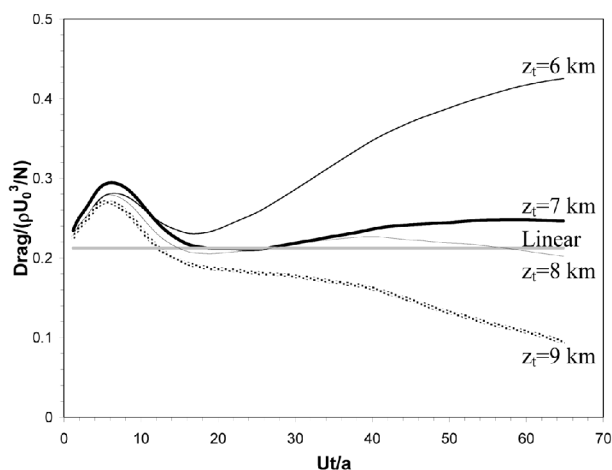


Figure 14. Time evolutions of the normalized pressure drag for the experiments without heating and with the height of the top of the heating profile $z_t = 6, 7, 8$ and 9 km. The linear drag is denoted by the grey line.

from 7 to 6 km, and the top of the wave duct in the upstream descends from 5.25 to 4.5 km with a stability increase in the lower layer and a decrease in the layer immediately above. Once again these results highlight the significance of the modification of the environmental stability by latent-heat effects upstream of the crest. The results are generally consistent with the mid-level moisture case considered by Durran and Klemp (1982) that featured wave amplification through the reduction in the height of the wave-trapping interface. The fact that the wave amplitude increases as the depth of the lower stable layer is decreased and the stratification is increased, is suggestive of a transition to a severe windstorm state in a hydraulic fluid similar to that described by Smith (1985) and Durran (1986). In particular, the results for the simulations with upstream heating (Fig. 13) have many similarities with simulations of airflow over a mountain in a two-layer atmosphere in which the depth of the lowest layer of the fluid is varied, as shown in Fig. 5 of Durran (1986), and is indicative of supercritical and transcritical hydraulic-like behaviour.

Variations in the depth of the lowest layer of the fluid due to the changes in the upstream diabatic heating depth also lead to changes in the cross-mountain pressure drag:

$$D = \int_{-\infty}^{+\infty} p_s \frac{\partial h}{\partial x} dx,$$

where p_s is the surface pressure. The temporal evolution of the normalized drag is shown in Fig. 14. A steady state is not achieved for all of the simulations with heating, particularly for $z_t = 6$ and 9 km, because the heating continually modifies the mean state conditions. The pressure drag for $z_t = 6$ km doubles relative to the simulation without heating and the drag derived from linear theory for a single layer.

(d) Application of a nonlinear theory

In order to better understand the transition into the severe windstorm state that occurs as the depth of the heating profile is reduced (Fig. 13), the Smith (1985) nonlinear theory for severe downslope winds in a stratified, hydrostatic atmosphere is examined. We apply this theory to the region immediately in the lee of the mountain

TABLE 2. PARAMETERS FOR THE SMITH (1985) NONLINEAR RESONANCE THEORY DEDUCED FROM THE TWO-DIMENSIONAL HEATING EXPERIMENTS

z_t (km)	l (m^{-1})	\widehat{H}_o	\widehat{h}	\widehat{h}_c	$\widehat{\delta}_{cm}$
8	7.5×10^{-4}	4.9	0.60	1.00	0.0
7	8.0×10^{-4}	4.4	0.64	0.90	0.0
6	8.5×10^{-4}	3.6	0.68	0.52	-1.9

Here z_t is the top of the heating profile, l is the Scorer parameter, \widehat{H}_o is the non-dimensional layer depth, \widehat{h} is the non-dimensional topographic height, \widehat{h}_c is the non-dimensional critical topography height needed for nonlinear resonance, and $\widehat{\delta}_{cm}$ is the maximum non-dimensional critical streamline displacement.

where streamlines plunge dramatically and nonlinear effects are likely to be important (e.g. Smith 1976), and distinguish this wave response from the development of the non-hydrostatic lee-wave train that ensues downstream from the primary wave. The application of this theory to the idealized heating experiments is justified considering that the flow contains a stable layer near the surface and strong wind speeds in the lee beneath a well-mixed layer aloft, characteristics that are similar to the environment of the severe wind situation examined by Smith. In this theory, the height of the critical streamline originates upstream at $z = H_o$, and descends in the lee beneath the well-mixed layer. The flow below the critical streamline is described by Long’s (1955) hydrostatic equation such that the vertical displacement, $\delta_c(x)$, of the critical streamline is the solution of:

$$\widehat{h} = \widehat{\delta}_c \cos(\widehat{H}_o + \widehat{\delta}_c - \widehat{h}), \tag{7}$$

for a two-dimensional mountain, $\widehat{h}(x)$. The circumflex indicates that the variable is non-dimensionalized by the length-scale U/N . Smith (1985) presents graphical and numerical solutions for $\widehat{\delta}_c$ using (7) for specified \widehat{h} and \widehat{H}_o .

Computations of the maximum permanent streamline displacement in the lee, $\widehat{\delta}_{cm}$, are obtained through application of Smith’s (1985) theory to the idealized heating simulations; these are summarized in Table 2. The simulations with $z_t = 8$ and 7 km (Figs. 13(b)–(c)) contain a relatively deep lower stable layer. The theory indicates that for these two experiments, which are characterized by $\widehat{H}_o = 4.9$ and 4.4, respectively, the critical mountain height, \widehat{h}_c , is larger than \widehat{h} , and it follows that the critical streamline ascends and descends the topography without a permanent displacement or hydraulic transition (e.g. see Fig. 2 of Smith(1985)). However, for the $z_t = 6$ km experiment (Fig. 13(d)), \widehat{H}_o is 3.6 and \widehat{h} is sufficiently large relative to \widehat{h}_c so that a permanent streamline displacement occurs, with a $\widehat{\delta}_{cm}$ of -1.9 , which is equivalent to a streamline descent of 2.2 km in the lee. The Smith (1985) theory appears to be qualitatively useful in distinguishing the severe windstorm state that ensues with the $z_t = 6$ km experiment from the relatively weak wave response that occurs for the $z_t = 7$ and 8 km simulations. The estimated $\widehat{\delta}_{cm}$ for the $z_t = 6$ km experiment is 1.6 km (Fig. 13(d)), based on the simulated streamline altitude in the trough of the primary wave, which is in general agreement with the Smith (1985) theory. The sensitivity of Alpine flow to the depth of the heating can be understood by analogy with the sensitivity of river flow over an obstacle to the water depth. If the water is too deep, it is barely disturbed by the obstacle. If it is shallower, the water accelerates, drops and spills over the obstacle.

6. SUMMARY AND CONCLUSIONS

A series of large-amplitude trapped mountain waves were observed during a strong south-föhn event on 20 September 1999 (MAP IOP 2) in the lee of the Hohe Tauern range in the eastern Alps. The lee waves were observed *in situ* and by remote sensing instruments on board the NCAR Electra. Accurate estimates of the mean profiles of the static stability, winds, and moisture were obtained from multiple GPS dropsondes and radiosondes. These soundings are instrumental in quantitatively documenting a weak-stability layer aloft, which acts to reduce the Scorer parameter aloft and provide an environment conducive for partial gravity-wave ducting. Additionally, the profiles indicate that a layer 2 km deep is blocked upstream of the Hohe Tauern. The maximum vertical velocity magnitude is over 9 m s^{-1} with a corresponding 10 K potential-temperature perturbation. The dominant horizontal wavelength is approximately 15 km. The airborne SABL offers a unique depiction of the lee-wave structure through backscatter from attendant cloud features, and provides an independent estimate of the wave characteristics, such as the amplitude, wavelength, and steadiness, as well as the depth of the blocked layer.

A high-resolution nested nonlinear simulation (minimum $\Delta x = 1 \text{ km}$), conducted using COAMPS, is able to replicate the essential characteristics of the lee-wave event including the depth of the blocked layer and the weak-stability layer aloft. The model simulation captures many aspects of the lee-wave dynamics such as the dominant wavelength, maximum amplitude of the vertical velocity and potential-temperature perturbations, as well as the general decrease in wave amplitude with time in the later portion of the observing period. Power spectral density calculations confirm the accuracy of the model-simulated wavelength and amplitude. However, the wavelength of the primary lee wave is longer than that observed, probably due to inaccuracies in the modelled upstream conditions. The resonant wavelength of the trapped lee waves is accurately described by linear non-hydrostatic analytic solutions obtained using the Smith *et al.* (2002) model, however the amplitude is underestimated. The linear and nonlinear simulations suggest that the waves are only partially trapped, hence longer-wavelength modes are able to propagate vertically and subsequently amplify and overturn in the lower stratosphere.

A region of precipitation upstream of the Hohe Tauern crest, associated with synoptic-scale and forced orographic ascent (e.g. Smith *et al.* 2003), had a profound influence on the gravity-wave response. Real data and idealized nonlinear model simulations, non-hydrostatic linear analytic solutions, as well as application of the nonlinear resonance theory of Smith (1985) are applied to assess the impact of the latent-heat release upstream of the crest on the lee-side gravity-wave dynamics. The results from a three-dimensional nonlinear simulation performed without latent-heat release and cloud microphysical processes exhibit an increase in the static stability aloft and a reduction in the trapped waves. Linear non-hydrostatic analytic solutions confirm the importance of the weak-stability layer in the upper troposphere for trapping the wave. A series of two-dimensional nonlinear simulations, initialized with constant stratification and wind speed, were performed with a specified heating profile that is temporally invariant. The simulation results indicate that when the latent heating is confined to a relatively shallow layer, a nonlinear resonance occurs leading to a strong plunge of the airstream in the lee of the crest, and the solution evolves into a high-drag state. Thus, the latent-heat release upstream of the crest in this case promotes trapped waves through weakened stability in the upper troposphere, and tunes the atmosphere for nonlinear resonance resulting in strong descent in the lee, which reinforces the downstream lee-wave response.

The results of this study point to a number of challenges for the explicit prediction of mountain waves generated by complex topography, such as the Alps. The linear and nonlinear model simulations underscore the importance of proper representation of the low-level blocking forced by the local topography, such as Grossglockner, and aggregate effects of the larger-scale topography, such as the Alps, for accurate simulation of mountain waves. The nonlinear simulations clearly demonstrate that sufficient resolution is required to produce realistic simulations of lee waves over complex topography; in this case a horizontal grid increment of 1 km was needed. Mesoscale data assimilation resulted in an improved representation of the power spectral density relative to a model initialized with large-scale conditions, which highlights the importance of an accurate initial state for high-resolution prediction. The explicit simulation of gravity-wave launching, propagation, and breakdown over complex topography in the presence of multi-scale forcing, including upstream condensation and microphysical processes, remains a significant challenge.

ACKNOWLEDGEMENTS

The research support for the first author was provided by the Office of Naval Research (ONR) program element 0601153N. The support for the second author was provided by the National Science Foundation Grant ATM-0112354. We gratefully acknowledge the contribution of the MAP scientists, forecasters, staff, ATC and flight crews. Other members of the MAP gravity-wave breaking team, A. Broad, D. Fritts, K. Hoinka, J. Kuettner, G. Poulos, S. Smith and H. Volkert contributed greatly to the development flight observation strategy and the implementation of the flight tracks. This study would not have been possible without the contribution of the COAMPS development team, in particular S. Chen, R. Hodur, T. Holt, and J. Schmidt. Beneficial discussions with J. Teixeira contributed to this study. COAMPSTM is a trademark of the Naval Research Laboratory. Computing time was supported in part by a grant of HPC time from the Department of Defense Major Shared Resource Center, at Vicksburg, MS, and Aberdeen, MD.

REFERENCES

- | | | |
|---|------|---|
| Bougeault, P. | 1983 | A non-reflective upper boundary condition for limited-height hydrostatic models. <i>Mon. Weather Rev.</i> , 111 , 420–429 |
| Bougeault, P., Binder, P., Buzzi, A., Dirks, R., Houze, R., Kuettner, J., Smith, R. B., Steinacker, R. and Volkert, H. | 2001 | The MAP special observing period. <i>Bull. Am. Meteorol. Soc.</i> , 82 , 433–462 |
| Bretherton, F. P. | 1969 | Momentum transport by gravity waves. <i>Q. J. R. Meteorol. Soc.</i> , 95 , 213–243 |
| Broad, A. | 1996 | High-resolution numerical model integrations to validate gravity-wave drag parametrization schemes: A case-study. <i>Q. J. R. Meteorol. Soc.</i> , 122 , 1625–1653 |
| Chen, W.-D. and Smith, R. B. | 1987 | Blocking and deflection of airflow by the Alps. <i>Mon. Weather Rev.</i> , 115 , 2578–2597 |
| Doyle, J. D. and Shapiro, M. A. | 2000 | A multi-scale simulation of an extreme downslope windstorm over Norway. <i>Meteorol. Atmos. Phys.</i> , 74 , 83–101 |
| Doyle, J. D., Durran, D. R., Colle, B. A., Chen, C., Georgelin, M., Grubisic, V., Hsu, W. R., Huang, C. Y., Landau, D., Lin, Y. L., Poulos, G. S., Sun, W. Y., Weber, D. B., Wurtele, M. G. and Xue, M. | 2000 | An intercomparison of model predicted wave breaking for the 11 January 1972 Boulder windstorm. <i>Mon. Weather Rev.</i> , 128 , 901–914 |

- Doyle, J. D., Volkert, H., Dörnbrack, A., Hoinka, K. P. and Hogan, T. F. 2002 Aircraft measurements and numerical simulations of mountain waves over the central Alps: A pre-MAP test case. *Q. J. R. Meteorol. Soc.*, **128**, 2175–2184
- Durran, D. R. 1986 Another look at downslope windstorms. Part I: The development of analogs to supercritical flow in an infinitely deep, continuously stratified fluid. *J. Atmos. Sci.*, **43**, 2527–2543
- 1990 Mountain waves and downslope winds. Pp. 59–81 in *Atmospheric processes over complex terrain*. AMS Monograph 23. American Meteorological Society, Boston, USA
- Durran, D. R. and Klemp, J. B. 1982 The effects of moisture on trapped mountain lee waves. *J. Atmos. Sci.*, **39**, 2490–2506
- Hodur, R. M. 1997 The Naval Research Laboratory's Coupled Ocean/Atmosphere Mesoscale Prediction System (COAMPS). *Mon. Weather Rev.*, **125**, 1414–1430
- Klemp, J. and Durran, D. R. 1983 An upper boundary condition permitting internal gravity wave radiation in numerical mesoscale models. *Mon. Weather Rev.*, **111**, 430–444
- Klemp, J. and Wilhelmson, R. 1978 The simulation of three-dimensional convective storm dynamics. *J. Atmos. Sci.*, **35**, 1070–1096
- Kuo, Y.-H. and Anthes, R. A. 1984 Mesoscale budgets of heat and moisture in a convective system over the central United States. *Mon. Weather Rev.*, **112**, 1482–1497
- Lane, T. P., Reeder, M. J., Morton, B. R. and Clark, T. L. 2000 Observations and numerical modelling of mountain waves over the Southern Alps of New Zealand. *Q. J. R. Meteorol. Soc.*, **126**, 2765–2788
- Long, R. R. 1955 Some aspects of the flow of stratified fluids: III. Continuous density gradients. *Tellus*, **7**, 341–357
- Ogura, Y. 1984 'Response of cumulus clouds to large-scale forcing and cumulus parameterization'. FGGE Workshop, National Research Council, Woods Hole, Mass., USA
- Satomura, T. and Bougeault, P. 1994 Numerical simulation of lee wave events over the Pyrenees. *J. Meteorol. Soc. Jpn*, **72**, 173–195
- Scorer, R. S. 1949 Theory of waves in the lee of mountains. *Q. J. R. Meteorol. Soc.*, **75**, 41–56
- Shutts, G. 1992 Observations and numerical model simulations of a partially trapped lee wave over the Welsh mountains. *Mon. Weather Rev.*, **120**, 2056–2066
- Shutts, G. and Broad, A. 1993 A case-study of lee waves over the Lake District in northern England. *Q. J. R. Meteorol. Soc.*, **119**, 377–408
- Shutts, G. J. 1998 Stationary gravity-wave structures in flows with directional wind shear. *Q. J. R. Meteorol. Soc.*, **124**, 1421–1442
- Smith, R. B. 1976 The generation of lee waves by the Blue Ridge. *J. Atmos. Sci.*, **33**, 507–519
- 1979 The influence of mountains on the atmosphere. *Adv. Geophys.*, **21**, 87–230
- 1980 Linear theory of stratified hydrostatic flow past an isolated mountain. *Tellus*, **32**, 348–364
- 1985 On severe downslope winds. *J. Atmos. Sci.*, **43**, 2597–2603
- 1991 Kelvin–Helmholtz instability in severe downslope windstorm flow. *J. Atmos. Sci.*, **48**, 1319–1324
- 2001 Stratified flow over topography. Pp. 119–159 in *Stratified flows in the environment*. Ed. R. Grimshaw. Kluwer Publications, Dordrecht, the Netherlands
- Smith, R. B., Skubis, S. T., Doyle, J. D., Broad, A., Kiemle, C. and Volkert, H. 2002 Mountain waves over Mt. Blanc: Influence of stagnant boundary layer. *J. Atmos. Sci.*, **59**, 2073–2092
- Smith, R. B., Jiang, Q., Fearon, M. G., Tabary, P., Dörninger, M., Doyle, J. D. and Benoit, R. 2003 Orographic precipitation and air mass transformation: An Alpine example. *Q. J. R. Meteorol. Soc.*, **129**, 433–454
- Vosper, S. B. and Mobbs, S. D. 1996 Lee waves over the English Lake District. *Q. J. R. Meteorol. Soc.*, **122**, 1283–1305